Defect patterns of two-dimensional nematic liquid crystals in confinement

Xiaomei Yao and Lei Zhang [*]
Beijing International Center for Mathematical Research, Peking University, Beijing 100871, China

Jeff Z. Y. Chen [†]
Department of Physics and Astronomy, University of Waterloo, Waterloo, Ontario, Canada, N2L 3G1

(Received 29 October 2021; accepted 23 March 2022; published 15 April 2022)

A two-dimensional or quasi-two-dimensional nematic liquid crystal refers to a surface-confined system. When such a system is further confined by external line boundaries or excluded from internal line boundaries, the nematic directors form a deformed texture that may display defect points or defect lines, for which winding numbers can be clearly defined. Here, a particular attention is paid to the case when the liquid crystal molecules prefer to form a boundary nematic texture in parallel to the wall surface (i.e., following the homogeneous boundary condition). A general theory, based on geometric argument, is presented for the relationship between the sum of all winding numbers in the system (the total winding number) and the type of confinement angles and curved segments. The conclusion is validated by comparing the theoretical defect rule with existing nematic textures observed experimentally and theoretically in recent years.

DOI: 10.1103/PhysRevE.105.044704

I. INTRODUCTION

The bulk state of a nematic liquid crystal is a spatially uniform fluid with the long molecular axes spontaneously ordered in a common direction, for which a global nematic director can be defined. A familiar example is a nematic system composed of rodlike linear molecules, for which the bulk state can be described by a uniform nematic field in one direction. In an ideal nematic state, the field lines, similar to the field lines of a uniform electric field, extend in space. For a nonpolar system, the case considered here, these nematic field lines have no arrows (i.e., are head-to-tail symmetric) [1].

The introduction of a physical boundary, however, disrupts the otherwise uniform nematic field lines. Depending on how molecules are aligned at the boundary, this could create a frustration on the nematic field lines. When liquid crystal molecules prefer to align along the wall surface, a so-call "homogeneous" liquid crystal boundary surface is formed. The nematic field lines would then line up with the surface conditions and in the meantime, attempt to keep minimal field-line deformation to lower the distortion elastic energies. In a finite system, according to the physical conditions, the nematic field lines can form defect points, lines, etc.

For example, a well-studied problem is the structures formed by immersed colloid particles (spherical or other shapes) or dispersed liquid droplets in a liquid crystal. Tremendous experimental and theoretical progress has been made in the last two decades, devoting to understanding such systems [2–29]. The presence of colloid particle surfaces induces liquid crystal defects and in turn, the tendency of minimizing the overall liquid-crystal defect free-energy couples the colloid particles in a particular form, yielding, e.g., ordered three-dimensional colloidal crystals.

Another commonly studied example is a liquid crystal fluid confined to curved surfaces, which has drawn significant theoretical and experimental attentions in recent years. Depending on the geometry of the confining surface, the system may display both density and orientational field defects, which can be detected experimentally [30–36]. The nature of an ordered state depends on the geometric parameters as wells as how far the system is away from the isotropic-nematic transition. Commonly used examples in theories and computer simulations are the nematic defect structures formed by a two-dimensional (2D) fluid containing liquid-crystal molecules confined on a spherical surface [30,37–46] or a toroidal surface [47–53]. A number of theoretical and computer-simulation approaches have been taken to study nematic structures in confinement. The Frank elastic and Landau-de Gennes free-energy models are often used and contain phenomenological parameters [30,37–39,42,50,54–57]. The molecular-level based models, either the simpler Onsager and Maier-Saupe theories, or the more complicated density-functional theories, contain system parameters that can be traced back to the physical origins [43,44,46,58–63]. A universal mathematical theorem is such that the Euler characteristics of the confining manifold uniquely determine the total winding number associated with the liquid crystal defects. For example, the embedded director fields have either total winding number 2 or 0, for a spherical or toroidal surface, respectively.

Less, however, is understood about the general feature of another type of confinement. The past two decades have witnessed a surge in research activities on the topic of boundary-frustrated nematic states, when a liquid-crystal-like

[*] zhangl@math.pku.edu.cn
[†] jeffchen@uwaterloo.ca

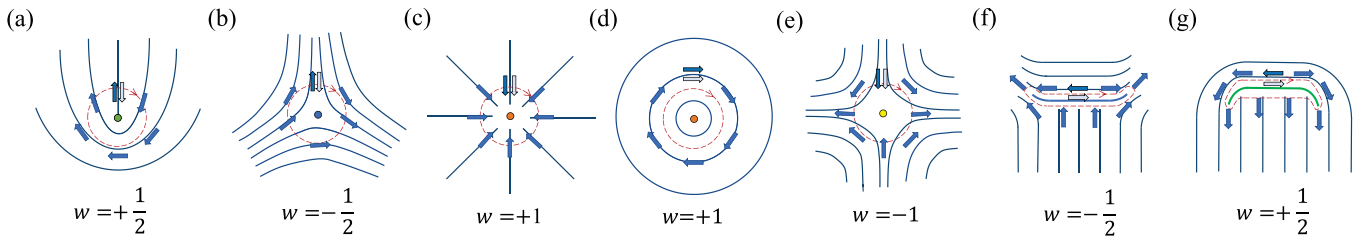

FIG. 1. Schematics of local defect types with winding numbers (a) $w = +1/2$, (b) $w = -1/2$, (c), (d) $w = +1$, (e) $w = -1$, (f) $w = -1/2$, and (g) $w = +1/2$, where panels (a)–(e) are patterns near defect points, and panel (f) as well as panel (g) patterns containing defect lines. The blue curves represent the directions of the (headless) nematic directors in space and the red dashed circles the path taken to evaluate the winding numbers. The same color scheme is used to illustrate the defect types in all the subsequent figures.

system in two dimensions is confined by a closed boundary line. These systems can be a flat square box containing traditional liquid crystal molecules [64], a collection of visible steel needles in circular and square boxes which are equilibrated by a vibrational bed [65], micron-sized gold particles of controlled shapes immersed in bulk liquid crystals [66], micron-sized rodlike colloid particles in confinement [67,68], or even semiflexible biological molecules confined in chambers of various shapes [69–71], all under physical conditions that can be classified as in quasi-2D. On the theoretical side, various theoretical approaches have been undertaken to model related systems, including solving Oseen-Frank (OF) model [70,72], Landau-de Gennes (LdG) model [64,73–78], and the density-functional theories such as the Onsager model [63,79,80] or beyond [68]. Monte Carlo (MC) simulations of confined rigid molecules in 2D or quasi-2D have also been made [71,81–87]. A rich variety of defect patterns have been obtained from these studies.

Hence, we face a fundamental question: how to set up a universal theory that can be used to explain the total defect winding number found in these 2D, line-confined systems, regardless of the experimental and theoretical methods used. The current paper serves two purposes. First, we derive the defect rules by using the characteristics of the confining boundaries. The simple case of a nematic fluid confined by an outer boundary is considered first in Sec. II, then followed by the case of a bulk nematic fluid containing an obstacle in Sec. III]. The general defect rule for more complicated confining geometries, also covering the above two cases, is then generalized in Sec. IV.

The second purpose is to comprehensively review the 2D nematic defect patterns discovered by various experimental, theoretical, and computer-simulation studies, in light of the defect rules that are deduced in this paper (see Sec. V A). As summarized in Table I, most of the boundary conditions used in these studies have the geometrical shapes of circles, triangles, rectangles, and hexagons. To supplement the existing studies, in Secs. II, III, and IV, we have provided the defect patterns obtained from numerical solutions to the Onsager model (see Appendix A), for more complicated confinement types. A comparison of the defect patterns produced from the studies listed in Table I and from our supplemented cases to the general defect rule determined in the current work verifies its validity.

II. TOTAL WINDING NUMBER INSIDE CONFINEMENT

A. Winding number of a single defect

For completeness, the definition of the winding number of a single defect is reviewed here. Figure 1 illustrates some basic types of local defect patterns, where the blue curves connect local nematic directors. A complete spatial path is taken about the defect, shown by the clockwise, dashed red circle. Although the nematic directors have the head-to-tail symmetry, blue arrows have been drawn for accounting purpose. As the red path completes its circle, the nematic director spins from the light blue arrow to the dark blue arrow; the spinning angle, in units of 2π, is defined as the winding number w. The sign of the winding number is positive if the arrow spins in the same direction as the red path, otherwise negative.

B. Total winding number of defects in confinement: Theory

The summed, total winding number of all defects of a nematic liquid crystal confined inside a polygon can be determined in a procedure similar to that in the last section. Instead of a local evaluation path around a defect point, for this purpose, we take a complete path inside the boundary of a polygon and evaluate the spinning of the nematic director.

The four basic types of nematic texture near polygonal corners are illustrated in Figs. 2(a)–2(d). At a length scale much greater than the molecular dimension, there are two typical nematic-director patterns, splay and bend, shown here in Figs. 2(a) and 2(b) inside an acute angle. As the evaluation red path passes around the corners, the nematic directors spin by angles $-\alpha_i$ and $\pi - \beta_j$, in Figs. 2(a) and 2(b), respectively. The indices i and j have been added to denote the ith and jth acute angles that contain splay and bend textures, correspondingly. In rare cases, the confinement geometry may contain a reflex angle, illustrated in Figs. 2(c) and 2(d), for two typical patterns, splay and bend. As the evaluation red path passes around a sharp boundary of a reflex angle, the nematic directors of the kth splay and lth bend patterns spin by angles $2\pi - \gamma_k$ and $\pi - \delta_l$, respectively.

Around the interior of the confinement, assume that there are n_1, n_2, n_3 and n_4 angles of type (a), (b), (c), and (d) in Fig. 2, and that the other molecules near the boundary are in parallel with the wall. The complete evaluation path takes all

TABLE I. Comparison between the defect rule, Eq. (9), and selected defect patterns found in the recent literature, of 2D systems that follow the same boundary conditions. The third column contains the figure numbers in the original references. M is the number of enclosed obstacles, N_1 and N_3 are splay related angles or extended angles if smooth curves are involved. W is the total winding number calculated from Eq. (9) and it matches the summed winding numbers of defects in the original figures.

Reference	Approach	Figure number(s)	Confinement type	M	N_1	N_3	W
Dzubiella2000 [81]	MC	16	Circle	0	0	0	1
Galanis2006 [65]	Experiment	4(a)	Square	0	2	0	0
		4(b), 4(c)	Circle	0	2	0	0
Tsakonas2007 [64]	LdG	3	Square	0	2	0	0
Galanis2010 [89]	Experiment	1(a)	Circle	0	0	0	1
Soares e Silva2011 [69]	Experiment	2	Square	0	4	0	−1
Evans2011 [66]	Experiment	4(c)	Triangle immersed	2	0	2	0
Luo2012 [90]	LdG	1	Square	0	2	0	0
Chen2013 [63]	Extended Onsager	1	Square	0	4	0	−1
		2	Circle	0	0	0	1
Lewis2014 [70]	OF	1	Rectangle	0	2	0	0
	Experiment	5(D, U_1)	Rectangle	0	2	0	0
	Experiment	5(D^*, U_1^*)	Rectangle	0	4	0	−1
de las Heras2014 [82]	MC	2(b), 2(c)	Circle	0	0	0	1
Geigenfeind2015 [91]	MC	12(b)	Square	0	4	0	−1
Gârlea2015 [83]	MC	2(b)	Square	0	4	0	−1
Gârlea2016 [84]	MC	1(e)	Circle	0	0	0	1
		1(g)	Circle	0	2	0	0
		2(a)–2(c)	Annulus	1	0	0	0
	Experiment	4(a)	Circle	0	0	0	1
		4(b)	Annulus	1	0	3	3/2
Everts2016 [73]	LdG	6, 7(e)–7(l)	Square	0	4	0	−1
Robinson2017 [74]	MC	2(b)right, 3 right, 4, 6	Square	0	4	0	−1
		5(a)	Square	0	2	0	0
	LdG	11(1–5, 10–12, 14, 15)	Square	0	2	0	0
		11(6)	Square	0	0	0	1
		11(7)	Square	0	4	0	−1
		11(8)	Square	0	3	0	−1/2
		11(9, 13)	Square	0	1	0	1/2
Cortes2017 [67]	Experiment	3(N)	Square	0	4	0	−1
Yao2018 [79]	Extended Onsager	3, 4, 7	Rectangle	0	4	0	−1
Wang2018 [75]	LdG	17(h)	Square-in-square	1	1	1	0
		17(m)	Square-in-square	1	2	3	1/2
		17(q)	Square-in-square	1	2	1	−1/2
Gârlea2019 [71]	MC	2(except H)	Circle and lens-shape	0	0	0	1
	Experiment	2(except H)	Circle and lens-shape	0	0	0	1
Hashemi2019 [86]	MC	1(b)–1(d), 3, 5(b)–5(d)	Circle	0	0	0	1
Hashemi2019 [85]	MC	1(b), 1(c), 2(b), 2(c), 3(c), 7	Square	0	4	0	−1
Yin2020 [76]	LdG	2(g) C±, I±	Square	0	0	0	1
		2(g) S, H, I, D	Square	0	2	0	0
		2(g)T	Square	0	3	0	−1/2
Han2020 [77]	LdG	4	Hexagon	0	0	0	1
	LdG	9	Hexagon	0	2	0	0
Han2021 [78]	LdG	2(a), 2(b)	Hexagon	0	0	0	1
		2(c), 2(d)	Hexagon	0	2	0	0
		5(c)	Triangle	0	3	0	−1/2

these basic types and gives rise to a total winding number

$$W = \frac{1}{2\pi}\left[\sum_{i=1}^{n_1}(-\alpha_i) + \sum_{j=1}^{n_2}(\pi - \beta_j) + \sum_{k=1}^{n_3}(2\pi - \gamma_k) + \sum_{l=1}^{n_4}(\pi - \delta_l)\right]. \quad (1)$$

According to the geometric theory, the total sum of all angles inside a polygon of any shape is $(n_1 + n_2 + n_3 + n_4 - 2)\pi$. This simplifies the above expression to

$$W = -\tfrac{1}{2}(n_1 - n_3 - 2), \quad (2)$$

which is one of the main results of the current paper. Note that W is determined by number of corners that contain splay patterns only.

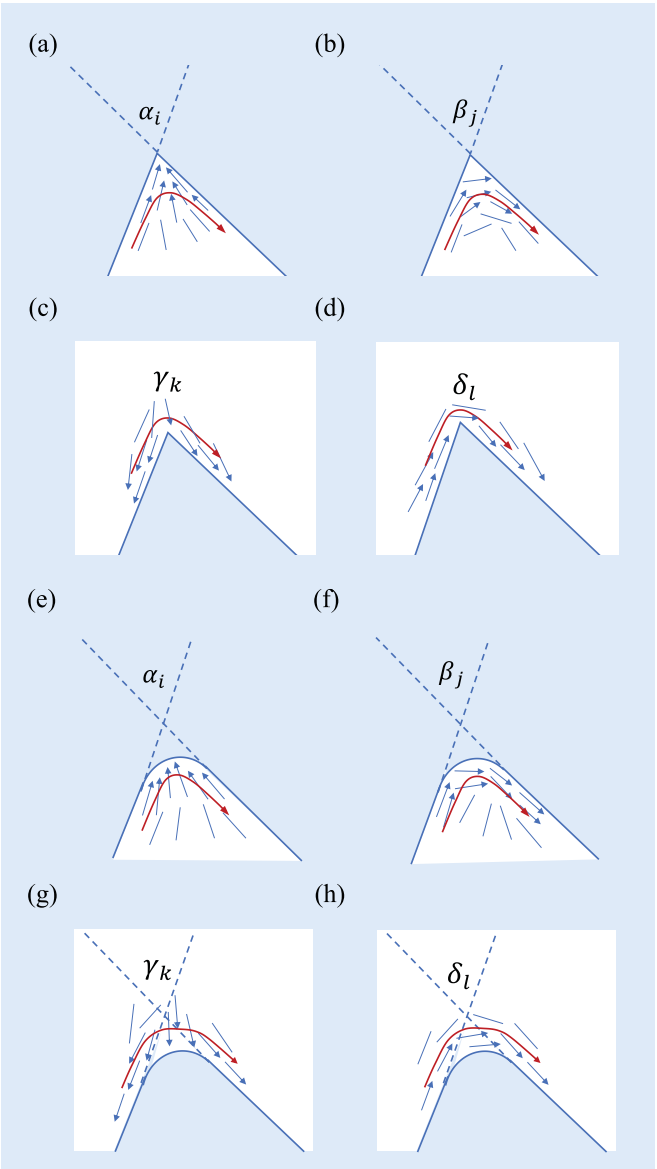

FIG. 2. Basic types of nematic textures, containing splay and bend patterns. Shown in panels (a) and (b) are acute confinement corners, α_i and β_j, that contain splay and bending textures; in panels (c) and (d) reflex corners, γ_k and δ_l, that contain splay and bend textures. Curved confinement segments in panels (e)–(h) can be dealt with by a similar definition, by extending the linear segments in connection with a typical curve, to form an acute or reflex angle.

One important generalization of the above expression is for nematic defects inside a closed boundary that is either completely composed of or partially contains a curve. Taking a curve segment, we can extend the tangent lines of the terminal ends of the curve to form a tangent angle, shown in Figs. 2(e)–2(h). Depending on the types of nematic textures near the curved boundary, e.g., splay or bend, the above formula can be directly used by counting number of splay patterns associated with these curves.

C. Examples

In an earlier publication [79], examples of confinement boundaries formed by acute angles, which were assumed to contain splay patterns only, and curve segments, which were assumed to contain bend textures only, were examined. In such a case, W in Eq. (2) has a simpler version: $W = -\frac{1}{2}(n_1 - 2)$ where n_1 is the number of acute angles of the confinement boundary. Section V C further addresses the consistency of how a splay or bend angle is identified.

Here, we demonstrate the usefulness of the expression in Eq. (2) by examining the examples from the numerical solutions to the extended Onsager model for lyotropic nematic liquid crystals under various types of confinement. The model is based on a classical free-energy model that Onsager developed for rodlike molecules of length L, interacting with each other through excluded-volume interactions [88]. The onset of the bulk nematic state, in which no spatial variations exist, depends on a single, reduced parameter

$$\tilde{\rho} = \rho_0 L^2, \tag{3}$$

where ρ_0 is the number of rodlike molecules per unit area. When the model is extended to include spatial dependence and effects of the boundary conditions, it can be effectively used to model a lyotropic liquid crystal in confinement, adding an additional system parameter

$$\tilde{L} = L/a, \tag{4}$$

where a is the typical size of the confinement geometry. More details can be found in Refs. [63,79,80] and Appendix A.

A comparison between the defect rule in Eq. (2) and the numerical solutions can be viewed in Fig. 3, where the first column displays the reconstructed defect patterns according to the density profile $\rho(\mathbf{r}, \mathbf{u})$, for direct visualization. The reduced density profile $\phi(\mathbf{r})$, averaged over all orientational dependence $\mathbf{u}$ and normalized by ρ_0, is a function of the spatial position specified by $\mathbf{r}$. Displayed in the second column, depletion of the density can be clearly viewed around the defect location. The orientational order parameter is assessed by the order parameter tensor $\mathsf{Q}(\mathbf{r})$ as a function of the spatial coordinates $\mathbf{r}$. In 2D, it is a 2×2 traceless and symmetric tensor,

$$\mathsf{Q}(\mathbf{r}) = \langle \mathbf{uu} - \mathsf{I}/2 \rangle = \frac{1}{2}\begin{bmatrix} S(\mathbf{r}) & T(\mathbf{r}) \\ T(\mathbf{r}) & -S(\mathbf{r}) \end{bmatrix}, \tag{5}$$

where I is a unit tensor. The right-hand side is the matrix representation of the tensor which contains the elements $S(\mathbf{r}) = \langle \cos 2\theta \rangle$ and $T(\mathbf{r}) = \langle \sin 2\theta \rangle$, θ being the angle that a rodlike molecule makes with respect to the horizontal axis. The average $\langle ... \rangle$ is performed with respect to the angular dependence θ only. The eigenvalue of the Q-tensor, $\Lambda = (S^2 + T^2)^{1/2}$, is plotted in the third row, in which a defect point shows up at a location where $\Lambda = 0$.

Among the plots, the circular and oval confinements in Figs. 3(a) and 3(b) are two interesting cases. They can be viewed as smooth curves with zero angles, hence all $n_1 = n_2 = n_3 = n_4 = 0$, which gives rise to $W = +1$ according to Eq. (2). In geometry, a circular shape could also be viewed as the asymptotic limit of a regular polygon when the polygon edge number approaches infinity. From the latter perspective,

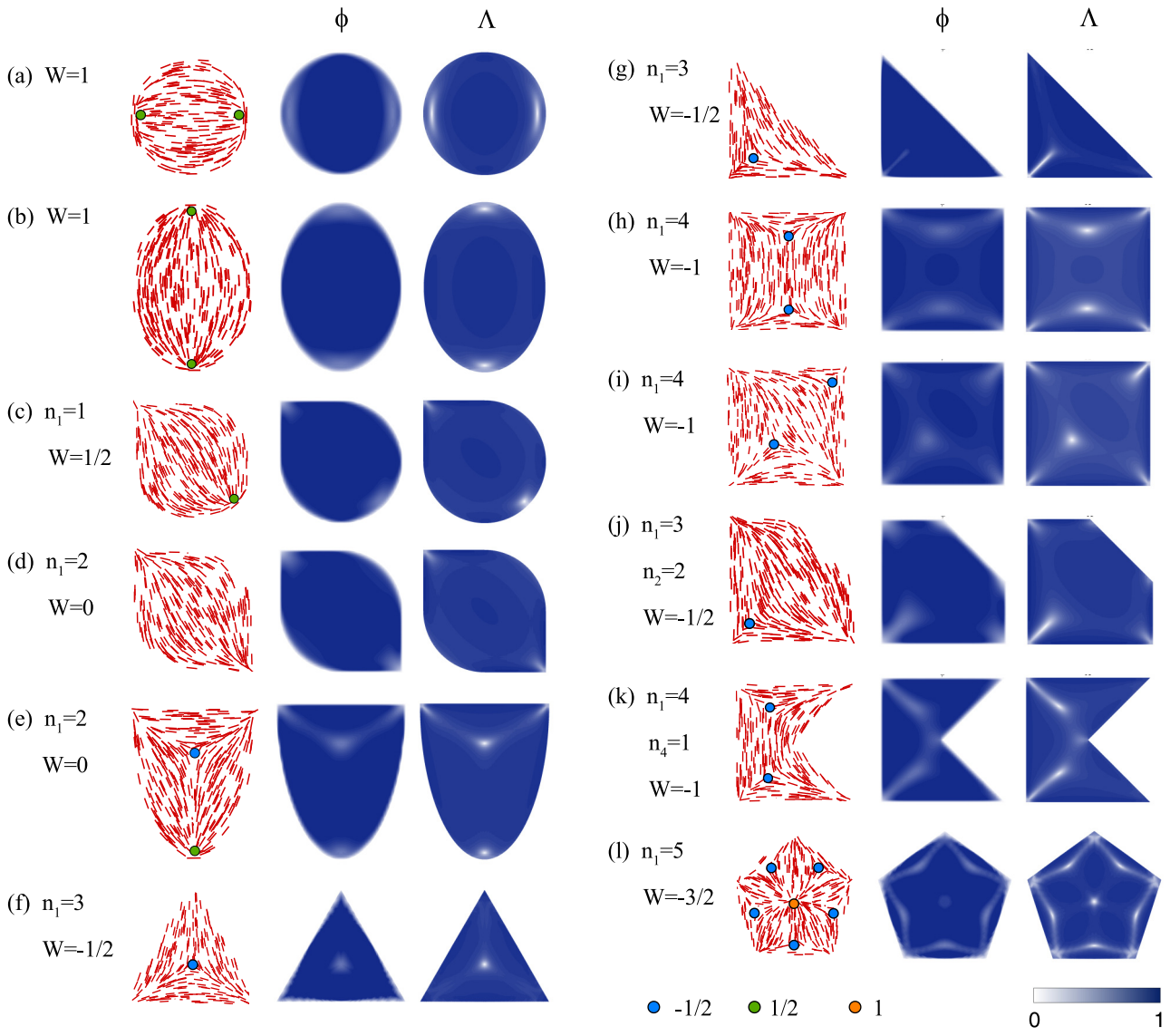

FIG. 3. Examples of defect patterns obtained from the solution to the extended Onsager model. The reduced density used is $\tilde{\rho} = 10$ and the reduced length $\tilde{L}$ in Eq. (4) is in the range [0.1, 0.25]. The first column contains reconstructed schematic plots based on the numerical solution presented in other columns, where the defect points are indicated by colored circles. The blue, green, and orange circles label the defect locations of $-1/2$, $+1/2$, and $+1$ winding numbers, respectively. The relative density $\phi(\mathbf{r})$ and orientational order parameter $\Lambda(\mathbf{r})$ are plotted in columns 2 and 3, respectively. The values of n_1, n_2, n_3, and n_4 are omitted when they are zero.

Fig. 3(a) corresponds to the case of $n_1 = n_3 = n_4 = 0$ but $n_2 \to \infty$; because the defect rule is not affected by the number of angles containing bend textures, $W = +1$.

The boundaries in Figs. 3(c)–3(e) consist of lines and curves, and those in Figs. 3(f)–3(l) contain polygonal segments. Most of the angles here are acute angles and liquid-crystal molecules prefer to align in splay patterns. In particular, there are two acute angles in Fig. 3(j) and a reflex angle in Fig. 3(k) around which the nematic liquids are in bend patterns. In short summary, the defect rule deduced based on geometry consideration is fully consistent with the numerical solutions from an actual molecular theory.

III. TOTAL WINDING NUMBER OF A NEMATIC LIQUID CONTAINING AN OBSTACLE

A. Total winding number of defects outside an obstacle: Theory

Here the case of a two-dimensional obstacle immersed in a nematic liquid is considered. The basic defect types in the liquid, near a corner angle or a curved boundary, are the same as those illustrated in Fig. 2.

Along the immediate exterior of the obstacle, a complete evaluation path encounters m_1, m_2, m_3, and m_4 patterns of the type α_i, β_j γ_k, and δ_l. The total winding number is hence the

same as in Eq. (1), that is

$$W = \frac{1}{2\pi}\left[\sum_{i=1}^{m_1}(-\alpha_i) + \sum_{j=1}^{m_2}(\pi - \beta_j) + \sum_{k=1}^{m_3}(2\pi - \gamma_k) + \sum_{l=1}^{m_4}(\pi - \delta_l)\right]. \quad (6)$$

The only difference is that the total sum of all angles outside a polygon of any shape is now $(m_1 + m_2 + m_3 + m_4 + 2)\pi$, which makes

$$W = -\tfrac{1}{2}(m_1 - m_3 + 2). \quad (7)$$

In comparison with Eq. (2), note the sign difference in front of 2. The total winding number is related to the number of angles (or the extended tangent angle from a curve segment) where the nearby liquid displays splay nematic patterns.

B. Examples

Solving the same extended Onsager model, we obtain the numerical solutions for the density profiles when differently shaped obstacles are immersed in an originally uniform nematic field. A few produced examples are displayed in Fig. 4, in which the values of m_1, m_2, m_3, and m_4 used in the above defect rule are also shown.

The circular obstacle in Fig. 4(a) has no angles, hence all m's vanish to yield $W = -1$. Though the obstacles in Figs. 4(b) and 4(c) contain a sharp angle, the nearby nematic liquid makes a bend pattern, hence $m_4 = 1$. The value of m_4, however, does not contribute to W in Eq. (7); this places them at the same category as Fig. 4(a) where $W = -1$.

The square obstacle in Figs. 4(d) and 4(e) has four corners but the nematic liquid around them has a bending texture. Hence $m_4 = 4$, which makes $W = -1$. The nematic defects in Fig. 4(d), though, are line defects, which can be contrasted with the defect points in Fig. 4(e).

Plots in Figs. 4(f) and 4(g) demonstrate that the geometric shape alone is not the determinant factor that decides the value of W. Both obstacles are triangles but are placed in the nematic liquid in different orientations. In Fig. 4(f), the nematic liquid around the two lower corners displays splay patterns, hence $m_3 = 2$; the upper corner is associated with a bend texture, which gives $m_4 = 1$. In total, according to Eq. (7), $W = 0$, which implies no defects in the nematic liquid. In Fig. 4(g), the right-hand-side angle is the only angle that is associated with a splay texture, hence $m_3 = 1$. The two on the left are associated with bend textures that give $m_4 = 2$. In total, using Eq. (7), we have $W = -1/2$, corresponding to a defect line in this case.

The obstacle in plot Fig. 4(h) has an interesting packman shape. Viewed from the nematic liquid, a splay pattern can be found near the acute angle in the center, and bend patterns near the two reflex angles on the right. This makes $m_1 = 1$ and $m_4 = 2$, therefore according to Eq. (7), the total winding number of the defects is $W = -3/2$; indeed, there are three $-1/2$ point defects in the system.

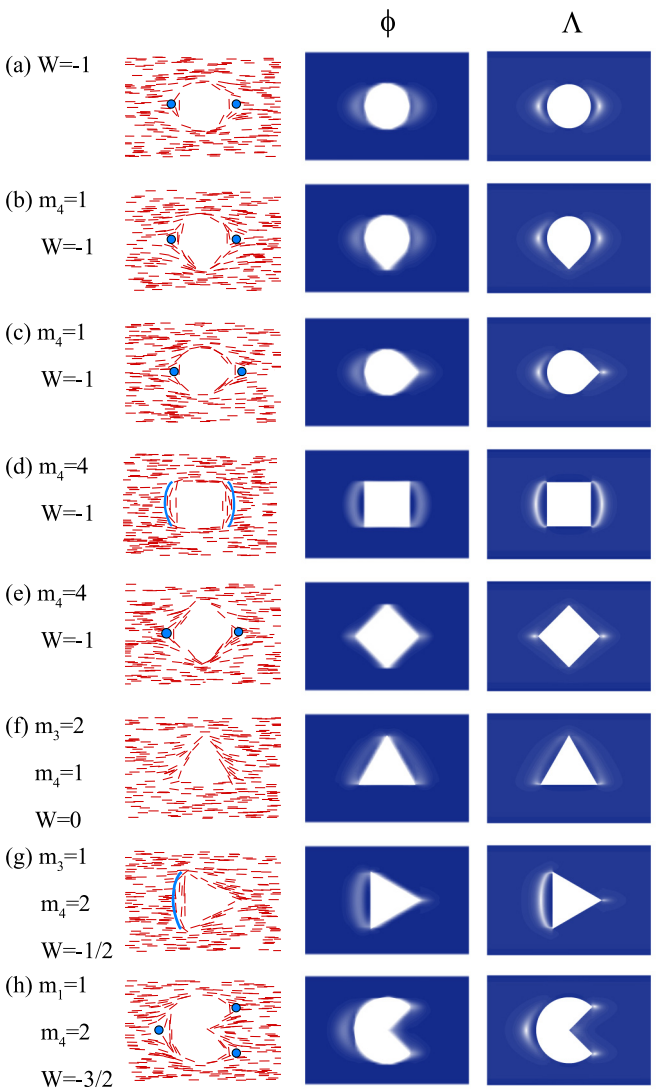

FIG. 4. Examples of defect patterns obtained from the solution to the extended Onsager model. The reduced density used is $\tilde{\rho} = 10$ and the reduced length $\tilde{L} = 0.06$, defined in Eq. (4). Colors used to indicate the defect points and gray scale used for the density plots have the same meanings as those in Figs. 2 and 3. The nonzero values of m_1, m_2, m_3 and m_4, together with the total W, are specified in each plot.

IV. TOTAL WINDING NUMBER OF A NEMATIC STATE OF A COMPLEX GEOMETRY

A. Theory

Finally, we generalize the above defect rules, Eqs. (2) and (7), to the case of a nematic liquid confined in a 2D boundary and containing obstacles. Inside the nematic liquid, there are M intruding obstacles of different shapes, forming different defect patterns nearby. These obstacles are labeled $l = 1, ..., M$. The rule for the total winding number can be easily deduced based on Eqs. (2) and (7). The sum of the two gives

$$W = -\frac{1}{2}\left\{(n_1 - n_3 - 2) + \sum_{l=1}^{M}\left[m_1^{(l)} - m_3^{(l)} + 2\right]\right\}, \quad (8)$$

where $m_1^{(l)}$ and $m_3^{(l)}$ are the number of acute and reflex angles associated with splay patterns of the lth obstacle, respectively.

Then, it gives a final,

$$W = -\tfrac{1}{2}(N_1 - N_3 + 2M - 2). \tag{9}$$

Here, N_1 is the total number of acute angles and N_3 total number of reflex angles, all related to splay patterns nearby. In case of the occurrence of a splay pattern at a curved boundary, an extended angle is constructed from the tangent lines at the terminal ends of a curve. The above rule could also be viewed as a general expression that contains both rules Eqs. (2) and (7). For example, letting $M = 0$ we return to Eq. (2). Regarding the boundaryless texture in the far field of Sec. IV as having a hypothetical, inverted boundary that does not contribute to the defect pattern, we return to Eq. (7) by letting $M = 1 + 1 = 2$, where the additional 1 takes the hypothetical boundary into account.

B. Examples

A number of examples from solving the extended Onsager model are shown in Fig. 5, mixing circular, triangle, and square boundary conditions in various forms. The total winding numbers in these examples are compared with the general theoretical prediction in Eq. (9).

The case of annularly confined liquid crystals is a recent topic of significant interest [68,80,84] [see Figs. 5(a) and 5(b)]. The wall boundaries enforce the liquid-crystal molecules to align along the wall direction, forming bend texture only. Hence $N_1 = N_3 = 0$. Taking $M = 1$ for a single obstacle, according Eq. (9), $W = 0$. The liquid crystal texture is then either defect-free [as in Fig. 5(a)] or has all defect winding numbers canceling each other [as in Fig. 5(b)]. While concentric boundaries are shown in Figs. 5(a) and 5(b), the above rule is also true for nonconcentric cases. The boundaries in Fig. 5(c) could be viewed as two nonconcentric circles asymptotically in tangent contact, hence $N_1 = N_3 = 0$, $M = 1$, which gives $W = 0$. They could also be viewed as forming a single boundary, for which we return to the theory in Sec. II, where two splay patterns exist ($n_1 = 2$), hence $W = 0$. Both analyses give the same W.

Though the center obstacle in Fig. 5(d) is a square, the liquid crystal pattern around all four corners is bend. According to Eq. (9), as it accounts for splay-related angles only, for $M = 1$ we have $W = 0$. The two pairs of $\pm 1/2$ defects in Fig. 5(d) cancel each other. From the perspective of having no splay-related angles, Fig. 5(d) is in the same class as Figs. 5(a)–5(c).

A contrasting case is Fig. 5(e), in which each corner of the central triangle accompanies a splay pattern, hence $N_3 = 3$. With $M = 1$, the defect rule Eq. (9) gives $W = 3/2$. The defect pattern in Fig. 5(e) clearly shows three $+1/2$ defect points.

Move now to a case where the liquid crystal is confined in a square and excluded from a small, concentric circle [see Fig. 5(f)]. Here, the four splay patterns near the square corners make $N_1 = 4$ and the central circle does not contribute to winding number counting. As the result, with $M = 1$ we have $W = -2$, which is the sum of the four $-1/2$ defects diagonally located inside the square.

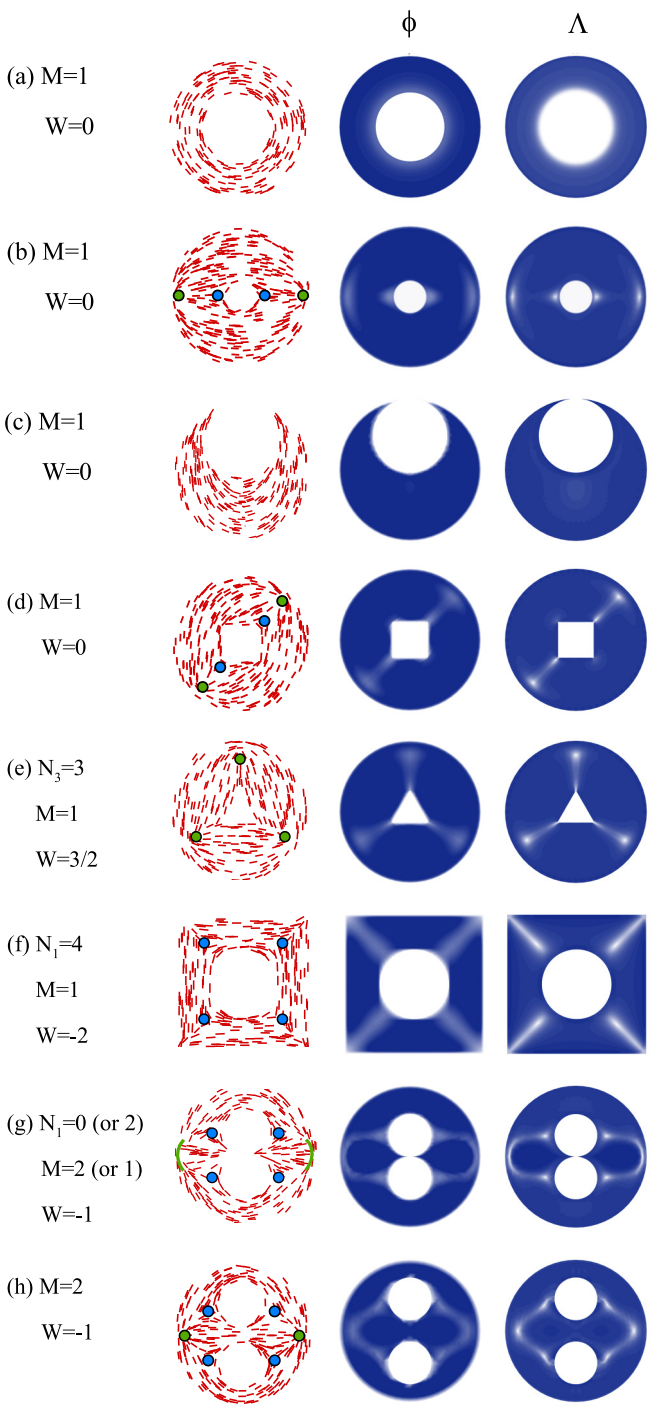

FIG. 5. Examples of defect patterns obtained from the solution to the extended Onsager model. The reduced density used is $\tilde{\rho} = 10$ and $\tilde{L}$ is selected in the range [0.1, 0.2]. Colors used to indicate the defect points and gray scale used for the density plots have the same meanings as those in Fig. 3. The nonzero values of N_1, N_3, and M, together with the total W, are specified in each plot.

The geometry in Fig. 5(g) can be assessed by two different methods. In the first one, it can be regarded as having the same geometry as the one in Fig. 5(h), with two inner circles separated from each other, but in this case, closely spaced. We then have $N_1 = N_3 = 0$ and $M = 2$, as can be clearly identified from Fig. 5(h). The defect rule Eq. (9) then gives $W = -1$.

On the other hand, the geometry in Fig. 5(g) can also be regarded as having one single obstacle ($M = 1$) which contains two splay-related acute angles ($N_1 = 2$). Either method makes $W = -1$, which is consistent with the properties of the six defect points and lines in Fig. 5(g).

V. DISCUSSION

A. Comparison with the literature

In the above, the defect rules of a confined nematic liquid are discussed in light of the solutions to the extended Onsager model as examples. The rules are quite general, independent of the actual theoretical or experimental approaches used in studying confined nematic liquids, as long as the liquid crystal molecules near a confinement wall prefer to align in parallel with the wall surface. Table I contains an incomplete list of some examples found in the literature and the comparison with our defect rules.

In this list, the type of the actual liquid-crystal "molecules" varies in a large range. The images of defect patterns were directly observed by crossed polarizers on liquid crystal E7, confined in square cells, which were compared to a LdG theory [64]. The observation of defect patterns of well-equilibrated, real macroscopic steel needles confined in square and circular cells was also made and compared to the solution of an OF theory [65,89]. Biomolecules are usually characterized by their semiflexibility; when confined in finite geometries, they also show nematic textures containing defect patterns [70,71,84]. A confocal-microscopy image of the nematic layer of micron-size rodlike colloid particles in a square well has also shown a pattern that contains defects [67].

In addition, the list includes the defect patterns produced from theoretical studies of the confined liquid-crystal systems. A short-cut to study the orientationally ordered state is the use of a model similar to the original OF theory [1,92]. Typically, the orientational properties are oversimplified by using a main-axis director field only, which is a unit vector field depending on the spatial location $\mathbf{r}$; the free energy is then proposed in terms of spatial derivatives of the vector field, where, at this stage, some of the anticipated orientational-ordering properties are taken into account. This has been one of the popular approaches to describe mechanical distortions (bend, splay, twist, etc.) of the director field in response to the external force. For confined liquid crystals, for example, OF theories have been used to explain some experimental observations [65,70,89].

The LdG theory for a system composed of rodlike molecules calls for the identification of a second-order, 3×3 order parameter tensor, in which elements are functions of $\mathbf{r}$. The LdG theory contains physical parameters associated with the elastic energy, typically depending on the molecular structure. A commonly used approximation is the one-coefficient approach, which erases the molecular identity and ignores, e.g., molecular flexibility of a molecule. The concept of the director field is not used in LdG originally and, instead, is produced as a result of the model. Incorporating the Dirichlet boundary conditions that enforces parallel alignment of the nematic directors at the confinement boundary, this has been a popular approach in recent studies of the liquid confinement problem [74,75,77,78,90].

A density functional theory (DFT) focuses on the probability distribution which is an inhomogeneous function of molecular orientation described by the unit vector $\mathbf{u}$ and molecular spatial arrangement described by $\mathbf{r}$. Various forms have been used for the liquid-crystal confinement problem, with incorporation of boundary conditions. For example, the extended Onsager model, which truncates the free-energy expansion beyond the second virial level, contains sufficient orientation-orientation interaction that describes a nematic state [63,70,79,80]; it can be regarded as a simple DFT. Built in a more complex form, the DFTs can effectively capture high-order virial terms and have been used recently for studying smectic liquid crystals in a quasi-2D confinement [68].

In addition to experimental and theoretical approaches, direct computer simulations of liquid crystal molecules in confinement have been taken. Typically, a liquid of anisotropically shaped molecules are placed in a confinement box; their positions and orientations are updated either according to the molecular dynamics or the Monte Carlo (MC) transition probability. Then, either snapshots or overall statistics can be collected. For a sensible comparison, only those configurations that follow the parallel homogeneous boundary patterns are included in this table [71,81–87].

As can be summarized in Table I, a rich variety of liquid-crystal defects have been produced either experimentally or theoretically. Regardless of the actual experimental systems and the theoretical approaches taken, all the defect patterns observed can be accounted for by our defect rules.

The systems included in the Table are those that can be classified as confined 2D or quasi-2D nematic liquid crystals on a flat surface. We have not included the systems of liquid crystals confined on curved surface (e.g., spherical or toroidal) [30–53], for which the winding-number property has long been established. Also not included in this Table are systems where nanoparticles or liquid droplets are immersed in 3D liquid crystals [2–29]; the additional dimension invalidates the basic assumptions made here for the 2D setting.

Closely related to the type of confinement studied here are those 2D and quasi-2D systems with homeotropic boundary conditions [93,94]; whether or not the approach taken here can be modified for the defect properties of these systems deserves further theoretical consideration. Recently, experimental studies of quasi-2D *smectic* liquid crystals confined by boundaries of various types of geometry have emerged. The displayed defects destroy both orientational ordering and smectic layering, which interwind with each other [68,87]. Emergent from a recent Monte Carlo study is the tetratic defects, which are carefully classified according to the confining boundary shapes in Ref. [87]. We have not included these sophisticated systems in the Table as they are beyond the simpler *nematic* assumption used for the defect rules considered here, although their boundary conditions are of the homogeneous type.

B. Other methods of counting the winding number

The total winding number W considered in this paper is based on the method of taking a calculation loop around the wall boundary and summing up the winding number of every

enclosed defects inside the loop. There are other methods of defining the total winding number.

In Refs. [74,78], for example, for a liquid crystal confined in a regular polygon of n sides, an addition contribution from every polygon corner is added to W. For square confinement, $n = 4$, Robinson *et al.* added a winding number $1/2 - 1/n = 1/4$ from a splay-associated corner and $-1/n = -1/4$ from a bend-associated corner to W. This makes the total winding number to be [74]

$$W' = W + n_1\left(\frac{1}{2} - \frac{1}{n}\right) - \frac{n_2}{n} = 0, \tag{10}$$

where $W = -(n_1 - 2)/2$ from Eq. (2) for $n_3 = 0$ is inserted to the above. The same $W' = 0$ was also used to explain the defect points observed by Han *et al.* for hexagonal confinement ($n = 6$). Now $1/2 - 1/n = 1/3$ from a splay-associated corner and $-1/n = -1/6$ from a bend-associated corner [78]. One could generalize this method even further for nonregular polygon confinement, which would always give a universal $W' = 0$.

To explain the defect patterns displayed from the MC simulations of hard ellipses confined by square boundary condition, Hashemi added four $+1/2$ winding numbers to W, each from a square corner. For four splay-associated corners, this makes $W'' = W + 4/2 = 1$, which is a value quoted in Ref. [85]. The reason for using such a W'' is unknown.

C. Splay or bend

The theory on the total winding number developed in Secs. II–IV depends on the identification of the number of acute and reflex angles associated with a splay pattern in the nematic fluid. Those with a bend pattern are not taken into account in the formulas. The classification of a bend pattern, however, deserves more detailed discussion.

The formation of the splay or bend patterns does not uniquely depend on the angle size. Although, usually the liquid crystals inside a sharp acute angle display a splay pattern. An example is given in Fig. 6(a) where the molecules are confined in a regular pentagon. Two and three angles are associated with splay and bend textures respectively, regardless of the fact that all angles by themselves are equivalent. Near angles A and B, the molecules prefer to fill the near-angle space in a splay pattern, to avoid density depletion near the angles, which would cost unwanted local depletion entropy. The density plot in Fig. 6(b) clearly demonstrates this fact near these angles. Near angles C, D, and E, the bend textures are clearly visible. The molecules near these angles need to make a compromise to accommodate the bend texture, by leaving the immediate area inside the angles unfilled. This affects the length scale of a several L, which is visible in the density plot. Although the density depletion costs the entopic term in the local free energies, the overall pattern over the entire fluid now has no defects, which is preferred by the total system free energy. Hence, the formation of the splay or bend patterns near an angle is completely determined by the balanced consideration of the total free energy.

Depending on the coarse-graining level, the classification of a splay- or bend-associated angle is not unique. Sometimes two different views can be taken. The example in Fig. 6(c) shows a bend pattern at the acute angle at a scale much greater than the molecular length, hence the angle is not accounted for in the defect formula. A second view gives a different accounting system, after observing at a molecular scale that the acute angle is actually associated with a splay pattern, which connects with a $-1/2$ defect point nearby. Using Eq. (2), an additional $-1/2$ is produced by adding an extra-1 to n_1 because of the splay-associated acute angle,

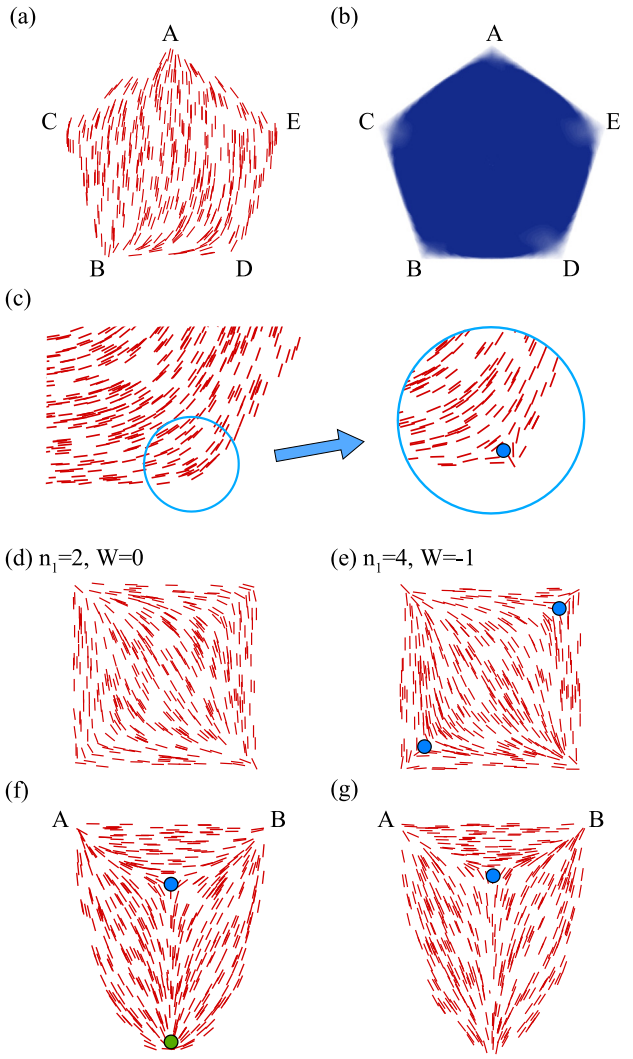

FIG. 6. Examples used for the discussion of splay and bend nematic textures. Plots (a) and (b) are the nematic-director map and the density profile, respectively, for a pentagon-confined rodlike liquid that has no interior defect. Plot (c) shows an example of a bend pattern in the zoom-out (coarse-grained) version, which is actually composed of a defect point and a splay pattern in the zoom-in (fine-grained) version. Plots (d) and (e) also demonstrate that two different views can be taken to view the bend-associated angles in plot (d). In plot (d), the two bend angles together with two splay-associated angles give an overall $W = 0$. In plot (e), all corners are associated with splay patterns, which give $W = -1$. Plots (f) and (g) are the nematic-director map of a nematic fluid confined in a shield-shape boundary, which have different degrees of resolution. In the fine-grained picture in panel (f), a defect is visible at the bottom and in the coarse-grained picture in panel (g), such a defect is invisible.

but this additional $-1/2$ is completely used to describe the $-1/2$ defect point close to the angle. Therefore, there are two ways of assessing this angle: either ignoring the defect in the zoom-out version by regarding this angle as a bend-textured angle, or in a zoom-in version by accounting for the defect and the splay-associated angle. Both give the correct total winding number counting.

Hence, a bend-associated acute angle can always be treated as a splay-associated acute angle with a hidden $-1/2$ defect point. If one takes this view, then n_1 in Eq. (2) could be regarded as the total number of acute angles of an confinement, and one simply has $W = -n_1/2 + 1$. On this basis, a seemingly bend-associated angle would need to be augmented by an invisible $-1/2$ defect point in using the above. It is this view that was taken in Sec. II(D) of Ref. [79]. For liquid crystal confined by a square boundary, examples in Figs. 6(d) and 6(e) further demonstrate the concept, which gives $W = 0$ (with two bend-associated angles) and $W = -1$ (with all splay-associated angles). Indeed, the confocal image of actin filaments in square confinement observed in Ref. [69] displays the texture similar to Fig. 6(d).

The interplay between splay and bend patterns can also manifest in another form. The example in Fig. 6(f) clearly has two splay-associated angles A and B hence $n_1 = 2$. Again, two different views can be taken for consideration of the defect near the bottom, curved boundary. The first view is to ignore the $+1/2$ defect point near the bottom curve, shown in Fig. 6(f) by the green circle. The entire pattern then looks like Fig. 6(g). According to the theory presented in Sec. II, now the curved segment has an extended tangent angle that is associated with a splay pattern, hence it adds to n_1 an additional 1: $n_1 = 2 + 1 = 3$. The formula in Eq. (2) then gives $W = -1/2$, which is fully consistent with the only defect point shown in Fig. 6(g). The second view gives a different accounting system, as illustrated in Fig. 6(f). The nematic fluid near the bottom curve has no singularity along the curved boundary, which produces an overall $W = 0$ for the interior defects, according to Eq. (2). Indeed, the sum of the winding number of the $+1/2$ defect (green circle in the figure) and the $-1/2$ defect (blue circle) gives $W = 0$. Both views are consistent in the winding number analysis. The fact that a $+1/2$ defect very close to a smooth bend curve can be regarded as a splay-associated, extended angle produces a simple method to account for the winding number: one takes all curves as bend curves and then associates a hidden $+1/2$ defect with a splay defect at the curved boundary. This method, the same as the second view presented for the example, was taken in Sec. II(D) of Ref. [79].

D. Extreme confinement

When the ratio between the molecular length and typical length-scale of confinement boundaries, L/a, exceeds a critical value, packing rodlike molecules in a finite confinement space dominates over the need to maximize the orientational entropy. The characteristic property of these extreme confinement systems is that the nematic directors along the confinement boundary no longer prefer parallel alignment. This was already observed in earlier granular-particle experiments [65,89], recent *fd*-virus packing experiments [71,84], and direct images of micron-sized colloidal particles [68]. One the theoretical side, Monte Carlo simulations [71,84] and the numerical solution to the extended Onsager model [80] have both demonstrated that these extremely confined liquid crystals are thermodynamically stable phases. Furthermore, concrete evidences [65], in particular a study of the free energy [80], all indicate that a phase transition exists between a usually confined state and an extreme state. It is unclear how the LdG theory, which typically requires a Dirichlet boundary condition, can be applied to model an extreme state.

The destruction of the homogeneous boundary condition precludes the basic assumption used in setting up the defect rules. The total winding number formulas developed in this work are based on the assumption of a continuous, space-filling nematic fluid, which is not applicable to the extreme nematic states.

VI. SUMMARY

Summing up all individual winding numbers of defect points and lines in a two-dimensional, confined nematic liquid crystal, how does it relate to the confining geometry formed by angles and curved segments? In this study, we deduced a general defect rule, which is applicable to a nematic liquid crystal having homogeneous boundary conditions. As we demonstrated above, the determinant factor is the number of splay-related angles and curved segments, whereas the bend-associated angles and curved segments do not contribute to the final result.

The general defect rule, Eq. (9), which includes the special cases in Eqs. (2) and (7), was then further validated by a comparison with results produced from experimental and theoretical studies in Sec. V A. While most of these studies concern systems composed of circular and polygon shapes, additional confinement types were also supplemented by considering the numerical solutions to the extended Onsager model, in Sects II, III, and IV.

The main focus of the current study is specifically on 2D liquid crystals confined by a closed line boundary. It fits into the much greater scope of the general topic of liquid crystals in confinement. Within the general topic, a well-established theorem is for liquid crystals confined on a curved and closed surface, such as on the spherical surface or toroidal surface, for which the total winding number formed by the defects in the liquid-crystal director lines is dictated by the Euler characteristics of the surface. Also within the general topic but for the specific confinement type of liquid crystals, on a flat surface and enclosed by a line boundary, the theory established in this paper is complementary to this theorem and consistently explains the variety of defect patterns observed in the recent literature.

ACKNOWLEDGMENTS

We acknowledge the financial support from the National Natural Science Foundation of China (Grants No. 21873009 and No. 12050002), the National Key Research and Development Program of China Grant No. 2021YFF1200500, and the Natural Sciences and Engineering Research Council of Canada.

APPENDIX A: EXTENDED ONSAGER MODEL

Assume that the distribution density function of finding the center of mass of rodlike molecules at a spatial position specified by the vector $\mathbf{r}$ with the condition that the rods point at the direction specified by the unit vector $\mathbf{u}$ is $\rho_c(\mathbf{r},\mathbf{u})$. It is normalized to n, the number of confined rodlike molecules in an area A, $\int d\mathbf{r}\int d\mathbf{u}\rho_c(\mathbf{r},\mathbf{u}) = n$. Accurate to the second-virial term [95], the free energy of the system can be written in a truncated Mayer expansion

$$\begin{aligned}\beta F = &\int \rho_c(\mathbf{r},\mathbf{u})\ln[L^2\rho_c(\mathbf{r},\mathbf{u})]d\mathbf{r}d\mathbf{u}\\ &+\frac{1}{2}\int \rho_c(\mathbf{r},\mathbf{u})w(\mathbf{r},\mathbf{u};\mathbf{r}',\mathbf{u}')\rho_c(\mathbf{r}',\mathbf{u}')\,d\mathbf{r}d\mathbf{u}d\mathbf{r}'d\mathbf{u}'\\ &+\int \rho_c(\mathbf{r},\mathbf{u})V_c(\mathbf{r},\mathbf{u})d\mathbf{r}d\mathbf{u}, \end{aligned} \tag{A1}$$

where $\beta = 1/k_BT$, with k_B being the Boltzmann constant and T the temperature. The first term represents the entropy of a spatially inhomogeneous and orientationally ordered fluid of rodlike molecules, where L^2 is included for dimensional convenience. The second term takes into account the interaction between two rodlike molecules having the coordinates $(\mathbf{r},\mathbf{u})$ and $(\mathbf{r}',\mathbf{u}')$, where the Mayer function $-w = \exp(-\beta v) - 1$. The interaction potential energy v between the two rigid molecules takes a value $v = \infty$ when the configuration of two rods overlap; $v = 0$ otherwise. The vector $\mathbf{u}$ is represented by the variables θ, the angle a rodlike molecule makes with respect to the horizontal axis.

The third term describes the interaction between rodlike molecules with an external potential energy. In the current application, $V_c = 0$ if the rodlike molecule has no overlap with a boundary wall, and $V_c = \infty$ if it does. Unlike the wall-potential for a small molecule where the orientation is not a concern, the rod-wall interaction depends on the orientation $\mathbf{u}$. In the numerical calculation, we used $V_c = 10^3$ instead of ∞, which effectively produces $\rho_c < 0.005$ when part of a rod overlaps with the wall. This masking technique is computationally efficient and requires no explicit specification of the boundary condition of $\rho_c(\mathbf{r},\mathbf{u})$. The expense, of course, is the need to careful specify $V_c(\mathbf{r},\mathbf{u})$ for a particular confinement shape.

In a much simpler mathematical problem, Onsager considered a trial-function solution of the model for a spatially homogeneous system (with $V_c = 0$) where $\rho_c(\mathbf{r},\mathbf{u})$ is a function of $\mathbf{u}$ only to demonstrate the existence of the nematic phase [88]. In 2D, one can take a bifurcation analysis and show that the second-order isotropic-nematic phase transition takes place when the 2D particle density $\rho_0 = n/A$ reaches a critical $\rho_0^* L^2 = 3\pi/2$ [96–98]. Most of $\tilde{\rho}$ values used here are well-above this critical density.

The reduced free energy in Eq. (A1) is the extended version of the Onsager model and contains $\mathbf{r}$-dependence. As a functional of the function $\rho_c(\mathbf{r},\mathbf{u})$, it needs to be minimized, by solving the stationary condition,

$$\frac{\delta F}{\delta\rho_c(\mathbf{r},\mathbf{u})} = 0. \tag{A2}$$

The actual calculation is conducted by mapping the current problem to the equivalent self-consistent field theory of a wormlike-chain system, where the chain rigidity is taken to be infinity [63,99]. The current numerical scheme used in solving the Green's formalism of the problem is identical to the procedure documented in an Appendix of Ref. [79], with the addition of an external energy as the masking potential to mimic the boundary condition.

APPENDIX B: VISUALIZATION OF THE STRUCTURES

In the text, a number of physical properties are analyzed and displayed, calculated from the distribution function of the center of mass of a rodlike molecule, $\rho_c(\mathbf{r},\theta)$, obtained from minimizing the free energy. One can deduce the distribution density function for segments on the rodlike molecules, regardless of the position on the rod, by defining

$$f(\mathbf{r},\mathbf{u}) = \frac{1}{\rho_0}\int_0^1 \rho_c\left[\mathbf{r} - \mathbf{u}L\left(s-\frac{1}{2}\right),\mathbf{u}\right]ds, \tag{B1}$$

where the distribution of the segments at the path coordinate s is traced back to the rod center. The integrant represents the probability density of finding the segment labeled by s on the rodlike molecule to appear at a location with the coordinate $\mathbf{r}$. With this definition, $f(\mathbf{r},\mathbf{u})$ is dimensionless.

A number of properties are calculated by using $f(\mathbf{r},\mathbf{u})$. The distribution density function for rod segments is calculated from

$$\phi(\mathbf{r}) = \int_0^{2\pi} f(\mathbf{r},\theta)d\theta, \tag{B2}$$

which is plotted in Figs. 3, 4, 5, and 6(b). The 2×2 Q-tensor,

$$\mathsf{Q}(\mathbf{r}) = \frac{1}{2}\begin{bmatrix} S(\mathbf{r}) & T(\mathbf{r}) \\ T(\mathbf{r}) & -S(\mathbf{r})\end{bmatrix}, \tag{B3}$$

is calculated from

$$S(\mathbf{r}) = \frac{\int_0^{2\pi} d\theta\cos(2\theta)f(\mathbf{r},\theta)}{\phi(\mathbf{r})}, \tag{B4}$$

$$T(\mathbf{r}) = \frac{\int_0^{2\pi} d\theta\sin(2\theta)f(\mathbf{r},\theta)}{\phi(\mathbf{r})}. \tag{B5}$$

Both S and T characterize the orientational ordering of the rodlike molecules by themselves and can be used directly. The scalar orientational order parameter is determined by the positive eigenvalue of the Q-tensor,

$$\Lambda(\mathbf{r}) = \sqrt{S^2(\mathbf{r}) + T^2(\mathbf{r})}, \tag{B6}$$

which is plotted in Figs. 3–5. Particularly, the locations where $\Lambda \to 0$ are considered as the defect points.

[1] P. G. de Gennes and J. Prost, *The Physics of Liquid Crystals* (Clarendon Press, Oxford, UK, 1993).

[2] P. Poulin, H. Stark, T. C. Lubensky, and D. A. Weitz, Science **275**, 1770 (1997).

[3] V. G. Nazarenko, A. B. Nych, and B. I. Lev, Phys. Rev. Lett. **87**, 075504 (2001).
[4] I. Muševič, M. Škarabot, U. Tkalec, M. Ravnik, and S. Žumer, Science **313**, 954 (2006).
[5] M. Škarabot, M. Ravnik, S. Žumer, U. Tkalec, I. Poberaj, D. Babič, N. Osterman, and I. Muševič, Phys. Rev. E **76**, 051406 (2007).
[6] U. Ognysta, A. Nych, V. Nazarenko, I. Muševič, M. Škarabot, M. Ravnik, S. Žumer, I. Poberaj, and D. Babič, Phys. Rev. Lett. **100**, 217803 (2008).
[7] M. Ravnik, M. Škarabot, S. Žumer, U. Tkalec, I. Poberaj, D. Babič, N. Osterman, and I. Muševič, Phys. Rev. Lett. **99**, 247801 (2007).
[8] M. Škarabot, M. Ravnik, S. Žumer, U. Tkalec, I. Poberaj, D. Babič, N. Osterman, and I. Muševič, Phys. Rev. E **77**, 031705 (2008).
[9] M. Ravnik and S. Žumer, Soft Matter **5**, 4520 (2009).
[10] C. P. Lapointe, T. G. Mason, and I. I. Smalyukh, Science **326**, 1083 (2009).
[11] C. P. Lapointe, S. Hopkins, T. G. Mason, and I. I. Smalyukh, Phys. Rev. Lett. **105**, 178301 (2010).
[12] U. M. Ognysta, A. B. Nych, V. A. Uzunova, V. M. Pergamenschik, V. G. Nazarenko, M. Škarabot, and I. Muševič, Phys. Rev. E **83**, 041709 (2011).
[13] J. Dontabhaktuni, M. Ravnik, and S. Žumer, Soft Matter **8**, 1657 (2012).
[14] B. Senyuk, Q. Liu, S. He, R. D. Kamien, R. B. Kusner, T. C. Lubensky, and I. I. Smalyukh, Nature (London) **493**, 200 (2013).
[15] U. Tkalec and I. Muševič, Soft Matter **9**, 8140 (2013).
[16] M. A. Gharbi, M. Nobili, and C. Blanc, J. Colloid Interface Sci. **417**, 250 (2014).
[17] J. Dontabhaktuni, M. Ravnik, and S. Žumer, Proc. Natl. Acad. Sci. USA **111**, 2464 (2014).
[18] D. A. Beller, M. A. Gharbi, and I. B. Liu, Soft Matter **11**, 1078 (2015).
[19] B. Senyuk, Q. Liu, E. Bililign, P. D. Nystrom, and I. I. Smalyukh, Phys. Rev. E **91**, 040501(R) (2015).
[20] K. P. Zuhail and S. Dhara, Appl. Phys. Lett. **106**, 211901 (2015).
[21] A. Martinez, L. Hermosillo, M. Tasinkevych, and I. I. Smalyukh, Proc. Natl. Acad. Sci. USA **112**, 4546 (2015).
[22] S. M. Hashemi, U. Jagodič, M. R. Mozaffari, M. R. Ejtehadi, I. Muševič, and M. Ravnik, Nat. Commun. **8**, 14026 (2017).
[23] Y. Wang, P. Zhang, and J. Z. Y. Chen, Phys. Rev. E **96**, 042702 (2017).
[24] Y. Wang, P. Zhang, and J. Z. Y. Chen, Soft Matter **14**, 6756 (2018).
[25] Y. Yuan, G. N. Abuhaimed, Q. Liu, and I. I. Smalyukh, Nat. Commun. **9**, 5040 (2018).
[26] I. I. Smalyukh, Annu. Rev. Condens. Matter Phys. **9**, 207 (2018).
[27] Y. Zhou, B. Senyuk, R. Zhang, I. I. Smalyukh, and J. J. de Pablo, Nat. Commun. **10**, 1000 (2019).
[28] Y. Yuan, Q. Liu, B. Senyuk, and I. I. Smalyukh, Nature (London) **570**, 214 (2019).
[29] D. V. Sudhakaran, R. K. Pujala, and S. Dhara, Adv. Opt. Mater. **8**, 1901585 (2020).
[30] T. C. Lubensky and J. Prost, J. Phys. II **2**, 371 (1992).
[31] D. R. Nelson, *Defects and Geometry in Condensed Matter Physics* (Cambridge University Press, Cambridge, UK, 2002).
[32] A. Arsenault, S. Fournier-Bidoz, B. Hatton, H. Miguez, N. Tetreault, E. Vekris, S. Wong, S. M. Yang, V. Kitaev, and G. A. Ozin, J. Mater. Chem. **14**, 781 (2004).
[33] F. Li, W. C. Yoo, M. B. Beernink, and A. Stein, J. Am. Chem. Soc. **131**, 18548 (2009).
[34] M. J. Bowick and L. Giomi, Adv. Phys. **58**, 449 (2009).
[35] A. Fernández-Nieves, V. Vitelli, A. S. Utada, D. R. Link, M. Márquez, D. R. Nelson, and D. A. Weitz, Phys. Rev. Lett. **99**, 157801 (2007).
[36] T. Lopez-Leon, V. Koning, K. B. S. Devaiah, V. Vitelli, and A. Fernandez-Nieves, Nat. Phys. **7**, 391 (2011).
[37] D. R. Nelson, Nano Lett. **2**, 1125 (2002).
[38] M. Huber and H. Stark, Europhys. Lett. **69**, 135 (2005).
[39] G. Skačej and C. Zannoni, Phys. Rev. Lett. **100**, 197802 (2008).
[40] H. Shin, M. J. Bowick, and X. Xing, Phys. Rev. Lett. **101**, 037802 (2008).
[41] M. A. Bates, J. Chem. Phys. **128**, 104707 (2008).
[42] S. Dhakal, F. J. Solis, and M. Olvera de la Cruz, Phys. Rev. E **86**, 011709 (2012).
[43] W.-Y. Zhang, Y. Jiang, and J. Z. Y. Chen, Phys. Rev. Lett. **108**, 057801 (2012).
[44] W.-Y. Zhang, Y. Jiang, and J. Z. Y. Chen, Phys. Rev. E **85**, 061710 (2012).
[45] Y. Li, H. Miao, H. Ma, and J. Z. Y. Chen, Soft Matter **9**, 11461 (2013).
[46] Q. Liang, S. Ye, P. Zhang, and J. Z. Y. Chen, J. Chem. Phys. **141**, 244901 (2014).
[47] R. M. Evans, J. Phys. II **5**, 507 (1995).
[48] M. Bowick, D. R. Nelson, and A. Travesset, Phys. Rev. E **69**, 041102 (2004).
[49] R. L. B. Selinger, A. Konya, A. Travesset, and J. V. Selinger, J. Phys. Chem. B **115**, 13989 (2011).
[50] Y. Li, H. Miao, H. Ma, and J. Z. Y. Chen, RSC Adv. **4**, 27471 (2014).
[51] A. Segatti, M. Snarski, and M. Veneroni, Phys. Rev. E **90**, 012501 (2014).
[52] D. Jesenek, S. Kralj, R. Rosso, and E. G. Virga, Soft Matter **11**, 2434 (2015).
[53] S. Ye, P. Zhang, and J. Z. Y. Chen, Soft Matter **12**, 5438 (2016).
[54] P. Sheng, Phys. Rev. Lett. **37**, 1059 (1976).
[55] P. Sheng, Phys. Rev. A **26**, 1610 (1982).
[56] G. Napoli and L. Vergori, Phys. Rev. Lett. **108**, 207803 (2012).
[57] G. Napoli and L. Vergori, Phys. Rev. E **85**, 061701 (2012).
[58] A. Chrzanowska, P. I. C. Teixeira, H. Ehrentraut, and D. J. Cleaver, J. Phys.: Condens. Matter **13**, 4715 (2001).
[59] A. Chrzanowska, J. Comput. Phys. **191**, 265 (2003).
[60] D. de las Heras, E. Velasco, and L. Mederos, J. Chem. Phys. **120**, 4949 (2004).
[61] D. de las Heras, E. Velasco, and L. Mederos, Phys. Rev. E **79**, 061703 (2009).
[62] A. V. Emelyanenko, S. Aya, Y. Sasaki, F. Araoka, K. Ema, K. Ishikawa, and H. Takezoe, Phys. Rev. E **84**, 041701 (2011).
[63] J. Z. Y. Chen, Soft Matter **9**, 10921 (2013).
[64] C. Tsakonas, A. J. Davidson, C. V. Brown, and N. J. Mottram, Appl. Phys. Lett. **90**, 111913 (2007).
[65] J. Galanis, D. Harries, D. L. Sackett, W. Losert, and R. Nossal, Phys. Rev. Lett. **96**, 028002 (2006).

[66] J. S. Evans, C. N. Beier, and I. I. Smalyukh, J. Appl. Phys. **110**, 033535 (2011).
[67] L. B. G. Cortes, Y. Gao, R. P. A. Dullens, and D. G. A. L. Aarts, J. Phys.: Condens. Matter **29**, 064003 (2017).
[68] R. Wittmann, L. B. G. Cortes, H. Löwen, and D. G. A. L. Aarts, Nat. Commun. **12**, 623 (2021).
[69] M. Soares e Silva, J. Alvarado, J. Nguyen, N. Georgoulia, B. M. Mulder, and G. H. Koenderink, Soft Matter **7**, 10631 (2011).
[70] A. H. Lewis, I. Garlea, J. Alvarado, O. J. Dammone, P. D. Howell, A. Majumdar, B. M. Mulder, M. P. Lettinga, G. H. Koenderink, and D. G. A. L. Aarts, Soft Matter **10**, 7865 (2014).
[71] I. C. Gârlea, O. Dammone, J. Alvarado, V. Notenboom, Y. Jia, G. H. Koenderink, D. G. A. L. Aarts, M. P. Lettinga, and B. M. Mulder, Sci. Rep. **9**, 20391 (2019).
[72] Y. Han, J. Yin, Y. Hu, A. Majumdar, and L. Zhang, Proc. R. Soc. A **477**, 20210458 (2021).
[73] J. C. Everts, M. T. J. J. M. Punter, S. Samin, P. van der Schoot, and R. van Roij, J. Chem. Phys. **144**, 194901 (2016).
[74] M. Robinson, C. Luo, P. E. Farrell, R. Erban, and A. Majumdar, Liq. Cryst. **44**, 2267 (2017).
[75] Y. Wang, G. Canevari, and A. Majumdar, SIAM J. Appl. Math. **79**, 1314 (2019).
[76] J. Yin, Y. Wang, J. Z. Y. Chen, P. Zhang, and L. Zhang, Phys. Rev. Lett. **124**, 090601 (2020).
[77] Y. Han, A. Majumdar, and L. Zhang, SIAM J. Appl. Math. **80**, 1678 (2020).
[78] Y. Han, J. Yin, P. Zhang, A. Majumdar, and L. Zhang, Nonlinearity **34**, 2048 (2021).
[79] X. Yao, H. Zhang, and J. Z. Y. Chen, Phys. Rev. E **97**, 052707 (2018).
[80] X. Yao and J. Z. Y. Chen, Phys. Rev. E **101**, 062706 (2020).
[81] J. Dzubiella, M. Schmidt, and H. Löwen, Phys. Rev. E **62**, 5081 (2000).
[82] D. de las Heras and E. Velasco, Soft Matter **10**, 1758 (2014).
[83] I. C. Gârlea and B. M. Mulder, Soft Matter **11**, 608 (2015).
[84] I. C. Gârlea, P. Mulder, J. Alvarado, O. Dammone, D. G. A. L. Aarts, M. P. Lettinga, G. H. Koenderink, and B. M. Mulder, Nat. Commun. **7**, 12112 (2016).
[85] S. Hashemi, Braz. J. Phys. **49**, 321 (2019).
[86] S. Hashemi, Braz. J. Phys. **49**, 44 (2019).
[87] P. A. Monderkamp, R. Wittmann, L. B. G. Cortes, D. G. A. L. Aarts, F. Smallenburg, and H. Löwen, Phys. Rev. Lett. **127**, 198001 (2021).
[88] L. Onsager, Ann. N.Y. Acad. Sci. **51**, 627 (1949).
[89] J. Galanis, R. Nossal, W. Losert, and D. Harries, Phys. Rev. Lett. **105**, 168001 (2010).
[90] C. Luo, A. Majumdar, and R. Erban, Phys. Rev. E **85**, 061702 (2012).
[91] T. Geigenfeind, S. Rosenzweig, M. Schmidt, and D. de las Heras, J. Chem. Phys. **142**, 174701 (2015).
[92] J. L. Ericksen, Arch. Rational Mech. Anal. **113**, 97 (1991).
[93] P. M. Phillips and A. D. Rey, Soft Matter **7**, 2052 (2011).
[94] M. R. M, R. K. Pujala, and S. Dhara, Sci. Rep. **9**, 4652 (2019).
[95] R. K. Pathria, *Statistical Mechanics* (Butterworth Heinemann, Oxford, UK, 1996).
[96] R. F. Kayser and H. J. Raveche, Phys. Rev. A **17**, 2067 (1978).
[97] J. A. Cuesta, C. F. Tejero, and M. Baus, Phys. Rev. A **39**, 6498 (1989).
[98] Z. Y. Chen, Phys. Rev. Lett. **71**, 93 (1993).
[99] J. Z. Y. Chen, Prog. Polym. Sci. **54-55**, 3 (2016).